PHYSICS

Tumbling and anomalous alignment of optically levitated anisotropic microparticles in chiral hollow-core photonic crystal fiber

Shangran Xie[1]*†, Abhinav Sharma[1,2†], Maria Romodina[1], Nicolas Y. Joly[1,2], Philip St. J. Russell[1,2]

The complex tumbling motion of spinning nonspherical objects is a topic of enduring interest, both in popular culture and in advanced scientific research. Here, we report all-optical control of the spin, precession, and nutation of vaterite microparticles levitated by counterpropagating circularly polarized laser beams guided in chiral hollow-core fiber. The circularly polarized light causes the anisotropic particles to spin about the fiber axis, while, regulated by minimization of free energy, dipole forces tend to align the extraordinary optical axis of positive uniaxial particles into the plane of rotating electric field. The end result is that, accompanied by oscillatory nutation, the optical axis reaches a stable tilt angle with respect to the plane of the electric field. The results reveal new possibilities for manipulating optical alignment through rotational degrees of freedom, with applications in the control of micromotors and microgyroscopes, laser alignment of polyatomic molecules, and study of rotational cell mechanics.

INTRODUCTION

It is well known that electrically polarized materials, when illuminated with laser light, experience a torque that tends to align their dipoles parallel to the electric field of the light, thus minimizing the free energy (*1*). This general principle is fundamental to a multitude of applications involving optical alignment, examples being molecular alignment for the control of chemical reactions (*2*), nematic liquid crystal alignment for optoelectronic displays (*3*), and rotational manipulation of biological cells for studying cell mechanics (*4*). In the context of optical levitation, it is known that positive uniaxial dielectric microcrystals, when trapped in a linearly polarized laser beam, experience an optical torque ($\boldsymbol{\tau}_A$)

$$\boldsymbol{\tau}_A = \int \mathbf{P} \times \mathbf{E} dV \quad (1)$$

where **E** is the applied electric field of the light, **P** is the anisotropic polarization, and the integral is over the particle volume *V*. This torque acts so as to reduce to zero the tilt angle between **P** and **E** (*5*, *6*), under which circumstances $\boldsymbol{\tau}_A$ vanishes. This phenomenon can also be used to orient birefringent particles or cause them to spin, depending on the polarization state of the light (*5*). Here, we report the observation of anomalous optical alignment effect on a rotating anisotropic microparticle levitated in the hollow core of a chiral photonic crystal fiber and driven by circularly polarized laser beams. The angular momentum introduced by the spinning causes the optical axis of the particle to tilt relative to the plane of the **E** field, in a manner analogous with precession of a top spinning under the influence of gravity. The chiral hollow-core photonic crystal fiber (HC-PCF) robustly preserves the circular polarization state of the trapping light, permitting control of the optical torque acting on the particle, and allowing its precession and nutation to be precisely monitored via the scattered light.

[1]Max Planck Institute for the Science of Light, Staudtstr. 2, 91058 Erlangen, Germany.
[2]Department of Physics, Friedrich-Alexander-Universität, Staudtstr. 2, 91058 Erlangen, Germany.
*Corresponding author. Email: shangran.xie@mpl.mpg.de
†These authors contributed equally to this work.

RESULTS

Vaterite microparticles with a mean diameter of 4.26 μm and a dispersion of 200 nm were used to demonstrate the effect. Vaterite is a positive uniaxial crystal with birefringence $\Delta n = n_e - n_o \sim 0.1$, where $n_e = 1.65$ and $n_o = 1.55$ are the refractive indices for light polarized along the extraordinary and ordinary axes. Scanning electron micrographs of the particles (Fig. 1A) reveal that they are nearly spherical with slight geometrical asymmetries (mean aspect ratio ~ 1.015, estimated by measuring individual particles in the right-hand picture) induced by the crystallization process, indicating the coexistence of (in general, nonaligned) optical and mechanical axes. A dual-beam trap formed within an HC-PCF was used to levitate and to drive particle rotation (Fig. 1B and see Materials and Methods for details). The HC-PCF was manufactured with a continuous chiral twist along its axis, causing the fundamental LP_{01}-like core mode to be circularly birefringent, thus allowing the circular polarization state of the trapping beams to be preserved (*7*). Chiral HC-PCF offers a convenient platform for exploring the full dynamics of the trapped vaterite particles.

First, the orientation of the optical axis of a trapped particle was confirmed to align with the direction of **E** field when linearly polarized trapping beams (at λ = 1064-nm wavelength) were launched from both fiber ends. Once the particle was trapped, the direction of **E** field for the trapping beams was rotated step by step using a half-wave plate (HWP), while the polarization state of probe light from a 632.8-nm He-Ne laser, scattered by the particle, was monitored (see fig. S2). The incident polarization of the probe beam was vertically polarized. The data in Fig. 1C show the measured Stokes parameter S_3 of the transmitted probe beam when the **E** field of the trapping beam was rotated from 0° to 180° in steps of 10° with respect to the probe polarization. The vertical bars mark the standard deviation (SD) in S_3 obtained after measurements on 10 different particles. A clear periodic variation of the S_3 parameter can be observed. The black dashed line in Fig. 1C plots the theoretical prediction using the value of $\Delta n = 0.09$ (see the Supplementary Materials). The good agreement confirms that the orientation of the optical axis follows the direction of **E** field in a linearly polarized trap (Fig. 1D) and that the effect of shape-induced birefringence (*8*) is negligible.

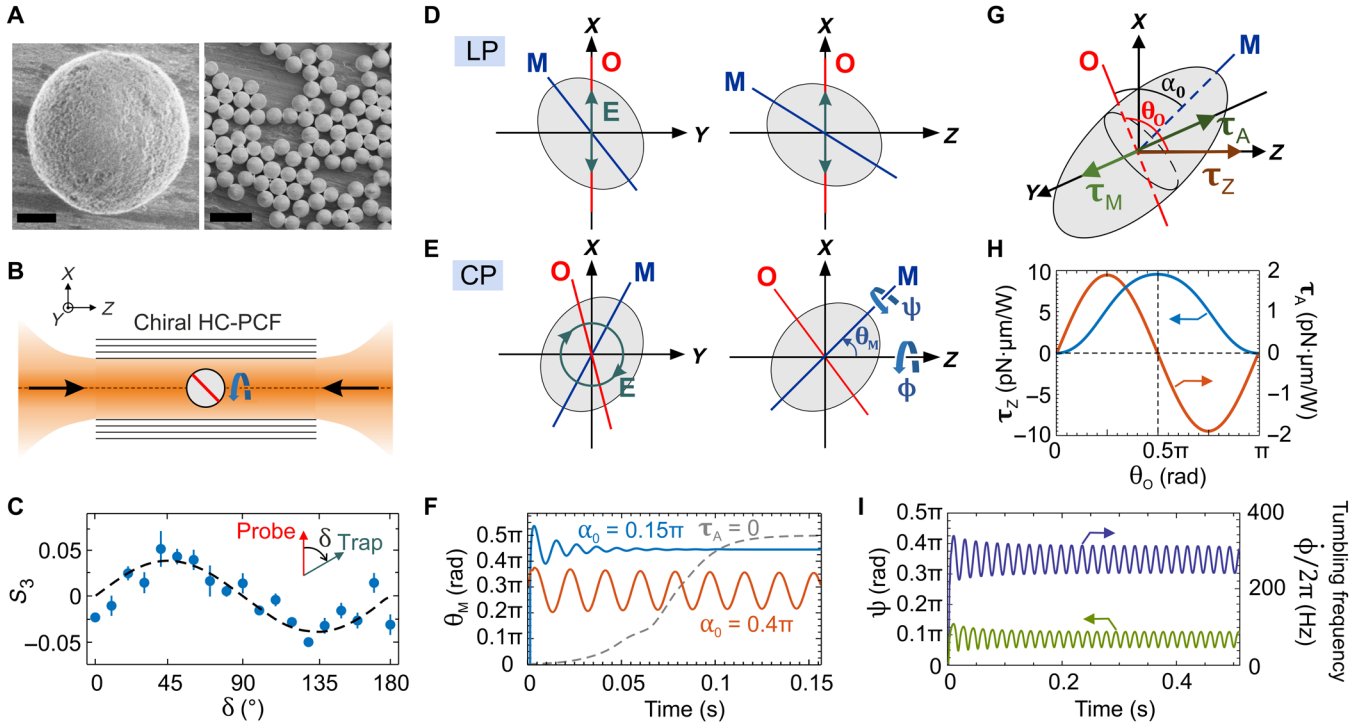

Fig. 1. Optical alignment and torque in levitated vaterite microparticles. (**A**) Scanning electron micrographs of vaterite particles. Scale bars, 1 μm (left) and 10 μm (right). (**B**) Sketch of a dual-beam trap formed within an air-filled chiral HC-PCF. (**C**) Measured Stokes parameter S_3 of the transmitted probe beam versus the angle δ between **E** field of the trapping beam and the input probe beam. The black dashed line shows the theoretical prediction using $\Delta n = 0.09$. (**D**) Alignment of optical axis (O) with **E** field when trapped in linearly polarized (LP) beams. Left and right panels are projections on the *XY* and *XZ* planes. The blue line marks the mechanical long axis (M). (**E**) Anomalous alignment of optical axis of a rotating birefringent particle trapped by circularly polarized (CP) beams. ϕ, ψ, and θ_M are the Eulerian angles, representing, respectively, tumbling, spinning, and nutational motion. (**F**) Calculated θ_M versus time under different conditions (see main text). (**G**) The optical rotation torque (τ_Z) is along *Z* axis. The optical (τ_A) and mechanical alignment (τ_M) torques lie in the *XY* plane and counterbalance each other. θ_O is the angle between extraordinary axis and *Z* axis, α_0 is the angle between optical and mechanical long axes. (**H**) Calculated τ_Z (blue) and τ_A (orange) versus θ_O. (**I**) Simulated tumbling frequency (blue) and spinning angle (green) overtime when $\alpha_0 = 0.4\pi$.

Anomalous optical alignment (Fig. 1E) occurred when the vaterite microparticle was made to spin by launching counterpropagating circularly polarized trapping beams (with opposite handedness so that the optical torques added up at the trapping site). In this situation, two types of optical torque play a role (Fig. 1G). One drives particle rotation around the beam axis (τ_Z), while the other tends to align the extraordinary axis into the plane of **E** field (τ_A). τ_Z arises from the altered polarization state of the light after scattering by the birefringent particle, which results in the transfer of spin angular momentum from the trapping beam to the particle. For a left-circularly polarized trapping beam incident on the particle in the +*Z* direction (the unit vector $\hat{\boldsymbol{Z}}$), $\boldsymbol{\tau}_Z$ can be written as (see the Supplementary Materials)

$$\boldsymbol{\tau}_Z = \frac{PB}{\omega}\hat{\boldsymbol{Z}}\left(1 - \frac{|E_L|^2 - |E_R|^2}{|E_L|^2 + |E_R|^2}\right) = \frac{PB}{\omega}\hat{\boldsymbol{Z}}\sin^2\left(\frac{2\pi R n_o}{\lambda}\left(1 - \frac{n_e}{\sqrt{n_o^2\sin^2\theta_O + n_e^2\cos^2\theta_O}}\right)\right) \quad (2)$$

where E_L and E_R are the left and right circularly polarized components of the scattered field, *P* is the optical power, ω is the optical frequency, *B* is the overlap between the trapping beam and the particle, *R* is the particle radius, and θ_O is the tilt angle between the optical axis and the *Z* axis (Fig. 1G). Symmetry considerations indicate that, no matter what the orientation of the particle, $\boldsymbol{\tau}_Z$ will point along the beam axis in the +*Z* direction for left circularly polarized light incident in the +*Z* direction and right circularly polarized light incident in the −*Z* direction. If there were no other effects, then this would cause the particle to spin about the fiber axis (tumbling motion) at a frequency $f_t = \dot{\phi}/2\pi$ that reaches a terminal value when the optical and viscous torques balance. However, there is also an alignment torque $\boldsymbol{\tau}_A$, which acts so as to rotate the optical axis of the particle into the transverse *XY* plane (see fig. S6). Figure 1H plots the calculated values of $\boldsymbol{\tau}_Z$ and $\boldsymbol{\tau}_A$ as a function of θ_O. As expected, $\boldsymbol{\tau}_Z$ vanishes when the optical axis is parallel to the beam axis ($\theta_O = 0$ or π) and reaches a maximum when $\theta_O = \pi/2$. In contrast, $\boldsymbol{\tau}_A$ vanishes when θ_O is π/2, and in the presence of viscosity, the system will stabilize at this position. Note that, unlike in single- or dual-beam traps created by tightly focused laser beams, when the steep transverse intensity gradient can cause elongated particles to experience an additional alignment torque (*9*, *10*), no such effect is observed in HC-PCF because of the much weaker intensity gradient of the diffraction-free fundamental mode in the hollow core [mode field radius of 10.2 μm, estimated using the capillary model (*11*)].

The full dynamics of particle motion can be described by solving the Euler equations in the frame of the particle

$$\dot{\mathbf{M}} + \boldsymbol{\Omega} \times \mathbf{M} + [\gamma]\mathbf{M} = \boldsymbol{\tau} = \boldsymbol{\tau}_A + \boldsymbol{\tau}_Z \quad (3)$$

where $\mathbf{M} = [\mathbf{I}]\boldsymbol{\Omega}$ is the angular momentum, $[\mathbf{I}]$ is the diagonal moment of inertia tensor, $\boldsymbol{\Omega}$ is the angular velocity, and $[\gamma]$ is a tensor representing rotational damping. Equation 3 can be numerically solved by expressing $\boldsymbol{\Omega}$ in terms of the time derivatives of the Eulerian angles θ_M, ϕ, and ψ (see the Supplementary Materials). The solutions show that, in addition to the optical torques, there is also a precessional torque $\boldsymbol{\tau}_M = \boldsymbol{\Omega} \times \mathbf{M}$ that tends to align the tilt angle of the mechanical long axis (θ_M) toward $\pi/2$, as shown by the gray dashed line in Fig. 1F for the case when $\boldsymbol{\tau}_A$ is set to zero in the model. This may also be understood as a centrifugal effect that pushes the "heavier" ends of the particle into the *XY* plane.

In the presence of all three torques, the steady-state Eulerian angles strongly depend on the angle α_0 between the optical and mechanical axes, which is randomly different for each particle. Figure 2A (left) plots the predicted equilibrium values of θ_O (orange) and θ_M (blue) against α_0 at 2 W of trapping power (1 W in each direction). It can be seen that, for the alignment and precessional torques to balance, θ_O and θ_M split from $\pi/2$ when $\alpha_0 \neq 0$ (*12*). As examples, Fig. 1F shows the temporal dependence of θ_M obtained by solving Eq. 3 with $\alpha_0 = 0.15\pi$ (blue) and 0.4π (orange). The particle undergoes damped nutation for $\alpha_0 = 0.15\pi$ and sustained nutation for $\alpha_0 = 0.15\pi$. The blue- and orange-shaded areas in Fig. 2A mark the root mean square amplitudes of θ_M resulting from the nutation. Through optomechanical back action, nutation changes the optical torque $\boldsymbol{\tau}$, modulating the instantaneous tumbling frequency and the spinning angle of the particle, as seen in the blue and green curves in Fig. 1I for $\alpha_0 = 0.4\pi$. Continuous spinning of the particle about its mechanical long axis is prohibited in the steady state, since, under these circumstances, the orientations of the optical and mechanical principal axes are optomechanically locked.

Changes in the alignment of the optical axis alter the optical torque $\boldsymbol{\tau}_Z$, directly influencing the tumbling frequency of the particle. The strong dependence of θ_O on the angle α_0, which is randomly different for each new particle, results in a wide range of possible tumbling frequencies (black line in Fig. 2A). The tumbling and nutation of a given vaterite particle can be monitored using a polarizer and a photodetector to measure the intensity and polarization state of light scattered sideways through the fiber cladding. Since the

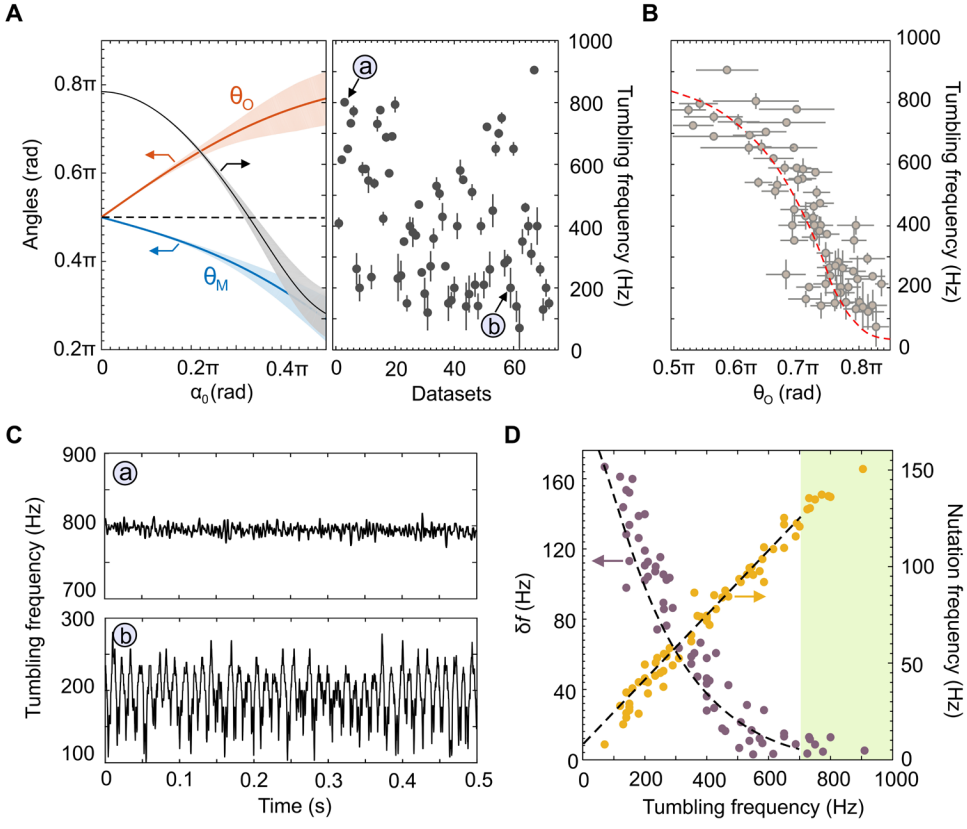

Fig. 2. Anomalous optical alignment, tumbling, and nutation of particle. (**A**) Left: Simulated orientations at equilibrium of the optical (θ_O, orange) and mechanical (θ_M, blue) principal axes, together with the corresponding tumbling frequency (black), plotted against α_0. The shaded areas mark the range over which these angles are modulated by particle nutation. Right: Measured steady-state tumbling frequency for 72 different vaterite particles at atmospheric pressure and a total power of 2 W. The vertical bars mark the nutation range for each particle. (**B**) Measured tumbling frequency versus θ_O. The red dashed line shows the theoretical prediction. (**C**) Measured tumbling frequency against time for cases *a* and *b* in (A). The visible periodic variation is induced by particle nutation. (**D**) Measured nutation frequency f_n (yellow) and tumbling frequency scatter δf_t (purple) plotted versus tumbling frequency for the same 72 particles. The black dashed line represents the best fit to solutions of the Euler equations (see the Supplementary Materials for free parameters). The green shaded area marks the region where particle nutation is damped out.

side-scattered light originates directly from the particle, it provides a highly sensitive means of monitoring its tumbling and nutation. Although, in principle, the signal transmitted through the fiber could also be used, it consists of a varying superposition of different guided modes that introduces intermodal interference and hard-to-predict uncertainties in intensity and polarization state. The tumbling frequency f_t can then be obtained by Fourier transforming the time-domain signal. Figure 2A (right) shows the measured values of f_t for 72 different particles of approximately the same diameter (SD, 200 nm) at atmospheric pressure and a trapping power of 2 W. The steady-state value of f_t varies from 100 Hz to more than 800 Hz, a range that is consistent with the predictions of the theory, but more than an order of magnitude greater than predicted by the dispersion in particle diameter (~60 Hz). To provide direct confirmation of this result, the value of θ_O was experimentally retrieved, using the blue curve in Fig. 1H, from the measured strength of the optical torque τ_Z, which was evaluated by extracting the peak-to-peak amplitude of the time domain signal collected at the transmitted end of fiber (see Materials and Methods). Figure 2B plots the measured tumbling frequency f_t against θ_O for the same 72 particles, as in Fig. 2A, showing that θ_O can be substantially different from $\pi/2$ and is directly linked to the tumbling frequency, as predicted by a theory (red dashed line). A histogram of the theoretically fitted values of angle α_0 for the 72 particles is shown in fig. S7.

The temporal variation in tumbling frequency f_t, detectable because of distortions in particle shape and the slight deviations from perfect sixfold rotational symmetry in the fiber core (see Materials and Methods), was calculated by applying a time-apertured Fourier transform to the measured time-domain signal. It is plotted in Fig. 2C for the particles marked *a* (top) and *b* (bottom) in Fig. 2A, and shows evidence of nutational motion. For particle (*b*), f_t is relatively low and the modulation in tumbling frequency δf_t (corresponding to the vertical bars in Fig. 2A, right) is rather high. Particle (*a*) has a higher value of f_t, nutation is strongly suppressed, and the modulation of the tumbling frequency is much smaller. Figure 2D plots the measured values of δf_t (purple) and nutation frequency f_n (yellow) versus f_t for all 72 particles, showing that when f_t is higher, nutation is quenched, while its frequency is higher. The measurements agree with the predictions of the Euler equations (black dashed lines; see the Supplementary Materials for the free parameters). The green-shaded area marks the region in which nutational motion fades away overtime in the model (see the blue curve in Fig. 1F as an example).

DISCUSSION

The particle orientation can be controlled over a wide range by varying the trapping power and the gas pressure. In Fig. 3A, the measured values of θ_O (dots) and f_t (squares) are plotted against total trapping power. As the power increases, τ_A rises linearly, and θ_O tilts toward $\pi/2$ but is prevented from reaching this value by the increase in precessional torque as the tumbling frequency increases. The value of α_0 (0.35π for the orange-coded data in Fig. 3A) is a free parameter in the model (see the Supplementary Materials) and can be estimated by fitting the measurements to solutions of Eq. 3 (green solid lines). For particles with $\alpha_0 = 0.06\pi$ (blue dots and squares), the measured values of f_t scale linearly with the trapping power since the optical and mechanical principal axes are almost parallel, and $\theta_O \sim \pi/2$. In this situation, no optomechanical alignment can be observed.

The squares in Fig. 3B show the measured tumbling frequency f_t as a function of gas pressure for the same particles, as in Fig. 3A (at 1-W trapping power). For both particles, f_t increases as the gas pressure falls, due to reduced viscous drag. For the particle with $\alpha_0 = 0.06\pi$ (blue), the measured value of f_t fits very well to the predictions when pressure-dependent rotational damping is included (black solid line; see the Supplementary Materials), indicating that in this situation, further increase in f_t is prevented by viscous damping. The measured values of θ_O (blue dots) are close to $\pi/2$. For the particle with $\alpha_0 = 0.35\pi$ (orange), f_t increases with reduced gas pressure, and θ_M approaches $\pi/2$ due to the rise in precessional torque. This induces a growth in θ_O that reduces the strength of τ_Z, further saturating the increase in f_t. At higher tumbling rates, since θ_M already reaches 0.5π, the increase in f_t is again dominated by the damping effect.

Our observation indicates that the optical alignment effect can be greatly tailored by adding rotational degrees of freedom into the system. By allowing full control of the rotational motions of optically levitated anisotropic particles, as is possible within the

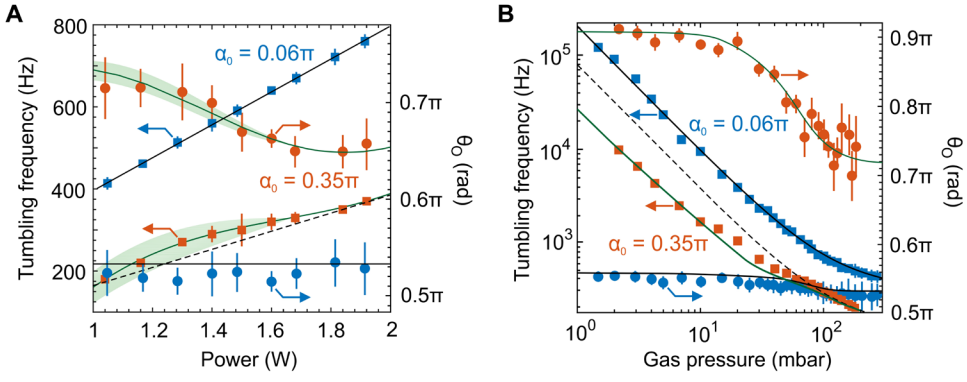

Fig. 3. Tuning of the particle orientation and the tumbling frequency. (**A**) Measured tilt angle θ_O (dots) and tumbling frequency f_t (squares) versus total trapping power for vaterite particles with angle $\alpha_0 = 0.35\pi$ (orange) and $\alpha_0 = 0.06\pi$ (blue). Green and black solid lines plot, respectively, the theoretical predictions using Eq. 3 when $\alpha_0 = 0.35\pi$ and 0.06π. The error bars and the shaded area are determined by the particle nutation. The black dashed line marks the linear relation to guide the eye. (**B**) Measured θ_O and tumbling frequency versus gas pressure for the same two particles as that in (A) at the trapping power of 1 W. The green and black solid lines are the simulation results. The black dashed line plots the predicted tumbling frequency purely determined by the pressure-dependent damping rate for the particle with $\alpha_0 = 0.35\pi$.

well-controlled confines of HC-PCF, all-optical alignment techniques can be significantly enhanced. The results have direct implications in applications involving levitated rotating microparticles, such as detection of ultraweak torques (*13*), probing the local ambient viscosity (*14*, *15*), quantum friction (*16*), Casimir forces (*17*), and testing material limits under centrifugal stress (*18*, *19*). They also introduce novel strategies for precision tuning of the orientation of levitated microspheres, indispensable for the realization of micromotors and microgyroscopes (*9*). The approach may also be useful in other contexts, such as laser-induced molecular alignment (*2*), nanostructure assembly (*20*), and rotational manipulation of biological particles (*21*–*23*).

MATERIALS AND METHODS

Experimental setup

The experimental setup for the dual-beam trap formed in a twisted HC-PCF is shown in fig. S1A. A continuous-wave laser beam at 1064-nm wavelength is split in two paths using a polarizing beam splitter and coupled into the LP_{01}-like core mode of the HC-PCF. Linear polarizers and quarter-wave plates are used to generate circularly polarized beams. The structure in the 6.1-cm-long twisted single-ring HC-PCF is chiral, with period 1.2 cm along the fiber axis. The measured near-field profile of a circularly polarized LP_{01}-like core mode is shown in fig. S1B, superimposed on a scanning electron micrograph of the cross section of the fiber.

To trap the vaterite particles (~4.26 μm in diameter), the power in the counterpropagating beams was balanced at the trapping site (left-hand end of the fiber in fig. S1A). Particle suspensions were created using a nebulizer and injected through an inlet tube positioned on top of the trapping site and aligned with the fiber endface (*24*). The mesh grid size of nebulizer was 6 μm, preventing the formation of clusters of particles. Once a particle was trapped in front of the fiber, the power of the beam from the left-hand side was increased to load the particle into the hollow core. Photodetectors (PDs) were installed to detect the transmitted (PD1) and side-scattered (PD2) light, so as to allow the particle motion and rotation to be monitored. Polarizers were mounted in front of the PDs to detect changes in the polarization state induced by particle rotation.

Experiment with linearly polarized trapping beam

Linearly polarized trapping beams were launched from both fiber ends to align the extraordinary axis of the trapped vaterite particles. The experimental setup is shown in fig. S2A. In this measurement, the orientation of the electric field of the trapping beam at 1064-nm wavelength was rotated by varying the angle of the two HWPs simultaneously. The orientation of the optical axis of the particle is expected to follow the electric field. The change in polarization state induced by particle rotation was probed by a He-Ne laser beam at 632.8-nm wavelength (with 2-mW optical power) that was coupled into the LP_{01}-like core mode using a dichroic mirror. The probe beam was vertically polarized, as was the initial polarization state of the counterpropagating trapping beams.

The rotation of the optical axis induces a maximum optical phase difference of $\sim 4\pi\Delta nR/\lambda_b$ between the ordinary and extraordinary probe beams, where Δn is the particle birefringence, R is particle radius, and λ_b is probe wavelength. The Stokes vector (normalized to the total power) of the signal transmitted through the fiber can be written as

$$\begin{pmatrix} S_1 \\ S_2 \\ S_3 \end{pmatrix} = (1-B)\begin{pmatrix} -1 \\ 0 \\ 0 \end{pmatrix} + B\begin{pmatrix} \cos^2\delta - \sin^2\delta \\ \sin(2\delta)\cos(4\pi\Delta nR/\lambda_b) \\ \sin(2\delta)\sin(4\pi\Delta nR/\lambda_b) \end{pmatrix} \quad (4)$$

where the angle δ is shown in fig. S2B. The first term on the right-hand side of Eq. 4 represents the transmitted amplitude of the unscattered light. The parameter B (~0.05) may be estimated by calculating the overlap between the particle and the LP_{01}-like core mode (*25*)

$$B = \int_0^R J_0^2(u_{01}\, r/R)\, 2\pi r dr \Big/ \int_0^a J_0^2(u_{01}\, r/a)\, 2\pi r dr \quad (5)$$

where a is the fiber core radius and u_{01} the first zero of the Bessel function J_0. Since the input probe beam was vertically polarized, the change in S_3 parameter was used to quantify the variation of the probe beam polarization induced by the rotation of the optical axis. Figure 1C shows the Stokes parameter S_3 of the transmitted probe beam (measured using a polarimeter) as the angle δ was rotated from 0° to 180° in steps of 10°. The vertical bars mark the SD obtained after measurements on 10 different particles. It is known that the effective birefringence of the uniaxial vaterite microparticles may slightly vary because of the process of crystal growing (*26*). The black dashed line in Fig. 1C plots the predictions of Eq. 4 using $\Delta n = 0.09 \pm 0.02$, which is consistent with the birefringence of bulk vaterite crystal (0.1).

Measurement of the orientation (θ_O) of the optical axis of the particle

The experimental setup is the same as fig. S1A. The orientation angle θ_O of the trapped particle can be retrieved from the measured optical rotation torque $\boldsymbol{\tau}_Z$ using the blue curve in Fig. 1H. The strength of $\boldsymbol{\tau}_Z$ was estimated using an approach similar to that reported in (*27*). The transmitted power at the fiber end (after a polarizer) was detected using an AC-coupled photodetector (PD1 in fig. S1A) with a transimpedance gain $G = 1.25$ kV/A. The detected voltage can then be written as

$$V_d = \frac{P \cdot G \cdot H \cdot B}{4}\left(1 - \frac{|E_L|^2 - |E_R|^2}{|E_L|^2 + |E_R|^2}\right)$$
$$\cos(2\dot{\phi}t) = \frac{\boldsymbol{\tau}_Z \omega G \cdot H}{4}\cos(2\dot{\phi}t) \quad (6)$$

where E_L and E_R are, respectively, the components of the Jones vector for the scattered field on the basis of left- and right-handed circular polarization, P is the optical power, ω is the optical frequency, H is the responsivity of PD1 (0.6 A/W), and $\dot{\phi}$ is tumbling angular frequency. It can be seen that the peak-to-peak amplitude of V_d can be directly correlated to the strength of $\boldsymbol{\tau}_Z$. Figure S3 plots the measured V_d for particles with tumbling frequency of 636.2 Hz (gray) and 193.9 Hz (orange), respectively. The total trapping power is $P = 2$ W. Note that the measured frequency is twice the particle tumbling frequency since the orientation of the particle optical axis repeats after its tumbling over 180° along the fiber axis. A clear difference in the signal amplitude between the two particles can be seen from the data. The estimated value of $\boldsymbol{\tau}_Z$ from the gray and orange curves is 17.9 ± 7.2 pN·μm and 6.8 ± 2.1 pN·μm, respectively, giving a θ_O of $0.62\pi \pm 0.09\pi$ (or $0.38\pi \pm 0.09\pi$) and $0.78\pi \pm 0.04\pi$

(or $0.22\pi \pm 0.04\pi$). The error bars are determined by the fluctuation in the peak-to-peak amplitude of V_d.

SUPPLEMENTARY MATERIALS

Supplementary material for this article is available at http://advances.sciencemag.org/cgi/content/full/7/28/eabf6053/DC1

REFERENCES AND NOTES

1. J. D. Jackson, *Classical Electrodynamics* (John Wiley & Sons, 2007).
2. H. Stapelfeldt, T. Seideman, Colloquium: Aligning molecules with strong laser pulses. *Rev. Mod. Phys.* **75**, 543–557 (2003).
3. W. M. Gibbons, P. J. Shannon, S.-T. Sun, B. J. Swetlin, Surface-mediated alignment of nematic liquid crystals with polarized laser light. *Nature* **351**, 49–50 (1991).
4. K. B. Roth, C. D. Eggleton, K. B. Neeves, D. W. M. Marr, Measuring cell mechanics by optical alignment compression cytometry. *Lab Chip* **13**, 1571–1577 (2013).
5. M. E. J. Friese, T. A. Nieminen, N. R. Heckenberg, H. Rubinsztein-Dunlop, Optical alignment and spinning of laser-trapped microscopic particles. *Nature* **394**, 348–350 (1998).
6. A. La Porta, M. D. Wang, Optical torque wrench: Angular trapping, rotation, and torque detection of quartz microparticles. *Phys. Rev. Lett.* **92**, 190801 (2004).
7. P. Roth, Y. Chen, M. C. Günendi, R. Beravat, N. N. Edavalath, M. H. Frosz, G. Ahmed, G. K. L. Wong, P. St.J. Russell, Strong circular dichroism for the HE_{11} mode in twisted single-ring hollow-core photonic crystal fiber. *Optica* **5**, 1315 (2018).
8. W. Singer, T. A. Nieminen, U. J. Gibson, N. R. Heckenberg, H. Rubinsztein-Dunlop, Orientation of optically trapped nonspherical birefringent particles. *Phys. Rev. E* **73**, 021911 (2006).
9. Y. Arita, M. Mazilu, K. Dholakia, Laser-induced rotation and cooling of a trapped microgyroscope in vacuum. *Nat. Commun.* **4**, 2374 (2013).
10. M. Rashid, M. Toroš, A. Setter, H. Ulbricht, Precession motion in levitated optomechanics. *Phys. Rev. Lett.* **121**, 253601 (2018).
11. J. C. Travers, W. Chang, J. Nold, N. Y. Joly, P. St.J. Russell, Ultrafast nonlinear optics in gas-filled hollow-core photonic crystal fibers [Invited]. *JOSA B* **28**, A11–A26 (2011).
12. Note that another set of solution on θ_O and θ_M in which both angles are mirrored about 0.5π is also accessible in the model by setting the proper initial conditions on the Eulerian angles. The two sets of solution are, however, not distinguishable in the experiment in terms of tumbling and nutation frequencies.
13. J. Ahn, Z. Xu, J. Bang, P. Ju, X. Gao, T. Li, Ultrasensitive torque detection with an optically levitated nanorotor. *Nat. Nanotechnol.* **15**, 89–93 (2020).
14. A. I. Bishop, T. A. Nieminen, N. R. Heckenberg, H. Rubinsztein-Dunlop, Optical microrheology using rotating laser-trapped particles. *Phys. Rev. Lett.* **92**, 198104 (2004).
15. Y. Arita, J. M. Richards, M. Mazilu, G. C. Spalding, S. E. Skelton Spesyvtseva, D. Craig, K. Dholakia, Rotational dynamics and heating of trapped nanovaterite particles. *ACS Nano* **10**, 11505 (2016).
16. R. Zhao, A. Manjavacas, F. J. García de Abajo, J. B. Pendry, Rotational quantum friction. *Phys. Rev. Lett.* **109**, 123604 (2012).
17. A. Manjavacas, F. J. Rodríguez-Fortuño, F. J. García de Abajo, A. V. Zayats, Lateral Casimir force on a rotating particle near a planar surface. *Phys. Rev. Lett.* **118**, 133605 (2017).
18. R. Reimann, M. Doderer, E. Hebestreit, R. Diehl, M. Frimmer, D. Windey, F. Tebbenjohanns, L. Novotny, GHz rotation of an optically trapped nanoparticle in vacuum. *Phys. Rev. Lett.* **121**, 033602 (2018).
19. J. Ahn, Z. Xu, J. Bang, Y. H. Deng, T. M. Hoang, Q. Han, R. M. Ma, T. Li, Optically levitated nanodumbbell torsion balance and GHz nanomechanical rotor. *Phys. Rev. Lett.* **121**, 033603 (2018).
20. O. M. Maragò, P. H. Jones, P. G. Gucciardi, G. Volpe, A. C. Ferrari, Optical trapping and manipulation of nanostructures. *Nat. Nano.* **8**, 807–819 (2013).
21. A. Ashkin, J. M. Dziedzic, Optical trapping and manipulation of viruses and bacteria. *Science* **235**, 1517–1520 (1987).
22. A. Ashkin, J. M. Dziedzic, T. Yamanet, Optical trapping and manipulation of single cells using infrared laser beams. *Nature* **330**, 769–771 (1987).
23. J. Wu, W. Zhang, J. Li, Bidirectional optical rotation of cells. *AIP Adv.* **7**, 085316 (2017).
24. A. Sharma, S. Xie, R. Zeltner, P. St.J. Russell, On-the-fly particle metrology in hollow-core photonic crystal fibre. *Opt. Express* **27**, 34496 (2019).
25. D. S. Bykov, S. Xie, R. Zeltner, A. Machnev, G. K. L. Wong, T. G. Euser, P. St.J. Russell, Long-range optical trapping and binding of microparticles in hollow-core photonic crystal fibre. *Light Sci. Appl.* **7**, 22 (2018).
26. S. J. Parkin, R. Vogel, M. Persson, M. Funk, V. L. Y. Loke, T. A. Nieminen, N. R. Heckenberg, H. Rubinsztein-Dunlop, Highly birefringent vaterite microspheres: Production, characterization and applications for optical micromanipulation. *Opt. Express* **17**, 21944–21955 (2009).
27. T. A. Nieminen, N. R. Heckenberg, H. Rubinsztein-dunlop, Optical measurement of microscopic torques. *J. Mod. Opt.* **48**, 405–413 (2001).
28. D. K. Hutchins, M. H. Harper, R. L. Felder, Slip correction measurements for solid spherical particles by modulated dynamic light scattering. *Aerosol Sci. Tech.* **22**, 202–218 (1995).

Acknowledgments

Funding: The work was funded by the Max Planck Society. **Author contributions:** S.X. conceived and supervised the research. S.X. and A.S. conducted the experiments. S.X., P.St.J. R., M.R., and N.Y.J. established the theoretical model. All authors contributed to data interpretation and manuscript preparation. **Competing interests:** The authors declare that they have no competing interests. **Data and materials availability:** All data needed to evaluate the conclusions in the paper are present in the paper and/or the Supplementary Materials.

Submitted 6 November 2020
Accepted 27 May 2021
Published 9 July 2021
10.1126/sciadv.abf6053

Citation: S. Xie, A. Sharma, M. Romodina, N. Y. Joly, P. St.J. Russell, Tumbling and anomalous alignment of optically levitated anisotropic microparticles in chiral hollow-core photonic crystal fiber. *Sci. Adv.* **7**, eabf6053 (2021).